Check for updates

Synthesis and adsorption properties of [Cu(L)$_2$(H$_2$O)]H$_2$[Cu(L)$_2$(P$_2$Mo$_5$O$_{23}$)]·4H$_2$O/Fe$_3$O$_4$ nanocomposites†

Ning Fang, Yu-Mei Ji, Chun-Yan Li, Yuan-Yuan Wu, Chen-Guang Ma, Hong-Ling Liu [ID] * and Ming-Xue Li*

Multifunctional [Cu(L)$_2$(H$_2$O)]H$_2$[Cu(L)$_2$(P$_2$Mo$_5$O$_{23}$)]·4H$_2$O/Fe$_3$O$_4$ (HL = pyridine-2-carboxamide) nanocomposites were successfully synthesized by combining [Cu(L)$_2$(H$_2$O)]H$_2$[Cu(L)$_2$(P$_2$Mo$_5$O$_{23}$)]·4H$_2$O and Fe$_3$O$_4$ nanoparticles. The characterization was performed by Fourier transform infrared spectroscopy (FTIR), transmission electron microscopy (TEM), vibrating sample magnetometry (VSM), X-ray powder diffraction (XRD) and ultraviolet-visible light absorbance spectrometry (UV-vis). The XRD and TEM analyses reveal that the nanocomposites possess high crystallinity with an average particle size of ∼19.43 nm. The VSM and UV-vis demonstrate excellent superparamagnetic behavior and two well-behaved absorption bands of the nanocomposites. The adsorption activity of the nanocomposites was investigated using methylene blue, gentian violet, safranine T, fuchsin basic, methyl orange and Sudan red (III) as probe molecules, and the results reveal that the [Cu(L)$_2$(H$_2$O)]H$_2$[Cu(L)$_2$(P$_2$Mo$_5$O$_{23}$)]·4H$_2$O/Fe$_3$O$_4$ nanocomposites have selective adsorption behavior for organic dyes. The recycling performance was observed using basic fuchsin, and the results demonstrate that the nanocomposites exhibit good recyclability and high stability. The [Cu(L)$_2$(H$_2$O)]H$_2$[Cu(L)$_2$(P$_2$Mo$_5$O$_{23}$)]·4H$_2$O/Fe$_3$O$_4$ nanocomposites have a promising future for magnetic, optical and biomedical applications.

1 Introduction

In recent years, polyoxometalate/nanoparticle nanocomposites (POMs/NPs) based on polyoxometalates and nanoparticles have attracted considerable interest due to their unique properties resulting from the combination of the polyoxometalates and the nanoparticles. Research has been dedicated to the fabrication of POMs/NPs with a wide variety of POMs and NPs such as α-K$_6$P$_2$W$_{18}$O$_{62}$/Pt, Na$_{12}$P$_2$W$_{15}$O$_{56}$·18H$_2$O/Pt, Na$_9$EuW$_{10}$O$_{36}$·32H$_2$-O/Pt, (NH$_4$)$_{14}$NaP$_5$W$_{30}$O$_{110}$·31H$_2$O/Fe$_3$O$_4$, H$_3$PW$_{12}$O$_{40}$/TiO$_2$, H$_6$P$_2$Mo$_{18}$O$_{62}$/TiO$_2$, [SiW$_9$V$_3$O$_{40}$]$^{7-}$/Bi$_2$O$_3$, and α-SiW$_{12}$O$_{40}$$^{4-}$/Ag to explore the synergistic properties arising from the nano-composites.[1–5] POMs/NPs have successfully been employed for biocatalysis,[6] electrocatalysis,[7] photocatalysis,[8] oxidation of alkenes,[9] bio-sensing,[10] and medicinal chemistry.[11] The assembly of POMs/NPs can provide a path for exhibiting their unique properties in many fields, and the complex structure makes them attractive for future study.

Polyoxometalates (POMs) are a well-known class of inorganic clusters consisting of a metal–oxygen framework, which have shown unique physicochemical properties and various applications owing to their highly electronegative and oxo-enriched surfaces, controllable shape and size, tunable acid–base, redox, magnetic, catalytic, and photochemical properties.[12–17] On the other hand, magnetic Fe$_3$O$_4$ nanoparticles are most widely known for their exceptional physicochemical properties, low cost, non-toxic nature as well as environmentally benign for industrial scale synthesis of fine chemicals.[18] The interdisciplinary integration of POMs and Fe$_3$O$_4$ nanoparticles has accelerated with fundamental curiosity and promising applications. Previously we have prepared Fe$_3$O$_4$ nanoparticles and their hybrids for the promising applications of heterogeneous catalysis, biological medicine, magnetofection, photo-therapy after magnetic separation, simultaneous photo-therapy and hyperthermia.[19–22] Herein, we report a facile route for the synthesis of [Cu(L)$_2$(H$_2$O)]H$_2$[Cu(L)$_2$(P$_2$Mo$_5$O$_{23}$)]·4H$_2$O/Fe$_3$O$_4$ nanocomposites using the ultrasonic technique.

Now, a large number of dye-waste water discharged pose a significant threat to the water environment and human health due to their toxicity and even carcinogenicity.[23] It is urgently-needed to find desirable adsorption materials, which not only reduce the pollutant organic dyes with high efficiency and low lost, but also realize selective separation and recovery. The use of nanomaterials as efficient catalysts in aqueous medium has

Henan Key Laboratory of Polyoxometalates, Institute of Molecular and Crystal Engineering, College of Chemistry and Chemical Engineering, Henan University, Kaifeng 475004, PR China. E-mail: hlliu@henu.edu.cn; limingxue@henu.edu.cn; Fax: +86-371-23881589

attracted considerable interests.[24,25] We investigated the adsorption of $[Cu(L)_2(H_2O)]H_2[Cu(L)_2(P_2Mo_5O_{23})]\cdot 4H_2O/Fe_3O_4$ nanocomposites using organic dyes such as methylene blue, gentian violet, safranine T, fuchsin basic, methyl orange and Sudan red (III) as probe molecules. The result reveals that the prepared $[Cu(L)_2(H_2O)]H_2[Cu(L)_2(P_2Mo_5O_{23})]\cdot 4H_2O/Fe_3O_4$ nanocomposites have selective adsorption behavior for organic dyes. The reusability of $[Cu(L)_2(H_2O)]H_2[Cu(L)_2(P_2Mo_5O_{23})]\cdot 4H_2O/Fe_3O_4$ nanocomposites as adsorbent is studied as well, and the results demonstrate that the $[Cu(L)_2(H_2O)]H_2[Cu(L)_2(P_2Mo_5O_{23})]\cdot 4H_2O/Fe_3O_4$ nanocomposites unveil good recyclability and high stability. Based on the experimental observations, the as-synthesized $[Cu(L)_2(H_2O)]H_2[Cu(L)_2(P_2Mo_5O_{23})]\cdot 4H_2O/Fe_3O_4$ nanocomposites could be treated as a promising adsorbent candidate. The outcomes prove that the new $[Cu(L)_2(H_2O)]H_2[Cu(L)_2(P_2Mo_5O_{23})]\cdot 4H_2O/Fe_3O_4$ nanocomposites could be of interest for fundamental studies and potential applications in magnetic, optical and biomedical filed.

2 Materials and methods

2.1 Materials

Copper(II) perchlorate hexahydrate $(Cu(ClO_4)_2\cdot 6H_2O,\ 98\%)$, pyridine-2-carboxamide $(C_{22}H_{17}ClN_2,\ 98\%)$, sodium molybdate dihydrate $(Na_2MoO_4\cdot 2H_2O,\ 99\%)$ and phosphoric acid $(H_3PO_4,\ 85\%)$ were purchased from J&K Scientific Ltd. Iron(II) acetylacetonate $(Fe(acac)_2,\ 99.9\%)$, poly(ethylene glycol)-*block*-poly(-propylene glycol)-*block*-poly(ethylene glycol) (PEO–PPO–PEO, M_n = 5800), octyl ether $(C_8H_{17}OC_8H_{17},\ 99\%)$, 1,2-hexadecanediol $(C_{14}H_{29}CH(OH)CH_2(OH),\ 90\%)$, DMF $(HCON(CH_3)_2,\ 99.5\%)$ and solvents such as hexane and ethanol were purchased from Aldrich. All materials were used as received without further processing. Distilled water was used throughout.

2.2 Synthesis of Fe_3O_4 nanoparticles

The Fe_3O_4 nanoparticles were synthesized according to the reported literature method.[19–22] A typical experiment was carried out in a 100 mL flask, 0.2541 g of iron(II) acetylacetonate, 0.7859 g of PEO–PPO–PEO as the surfactant, and 0.6468 g of 1,2-hexadecanediol were dissolved in 10 mL octyl ether under vigorous stirring. Subsequently, the reaction mixture was slowly heated to 125 °C within 1 h, homogenized for 1 h at 125 °C, then rapidly heated to 280 °C within 15 min and refluxed at the temperature for 1 h to complete the reaction. After cooling down to room temperature, the black precipitate products was washed with mixed solvents of ethanol/hexane ($V_{ethanol/hexane}$ is 2 : 1) several times, and re-dispersed in hexane for further use.

2.3 Synthesis of $[Cu(L)_2(H_2O)]H_2[Cu(L)_2(P_2Mo_5O_{23})]\cdot 4H_2O$

The $[Cu(L)_2(H_2O)]H_2[Cu(L)_2(P_2Mo_5O_{23})]\cdot 4H_2O$ was synthesized using the method similar as the literature method.[26–28] An aqueous solution containing $Cu(ClO_4)_2\cdot 6H_2O$ (0.093 g, 0.25 mmol) and pyridine-2-carboxamide (0.061 g, 0.5 mmol) was stirred at 50 °C for 0.5 h. After cooling to room temperature the solution was added to a 10 mL aqueous solution of $Na_2MoO_4\cdot 2H_2O$ (0.242 g, 1.0 mmol), the pH value was maintained at 3 by

dropwise adding of concentrated H_3PO_4 under continuous stirring. Then the mixture was stirred for 0.5 h and then filtered. By filtering the mixture, the powders were stored for the following synthesis. The filtrate was allowed to evaporate at room temperature. After 3 days blue crystals suitable for X-ray studies were filtered off, washed with distilled water and dried in a desiccator at room temperature to give a yield of 38.4% based on Mo. Anal calc. for $C_{24}H_{34}Cu_2Mo_5N_8O_{32}P_2$ (1615.30): C, 17.85; H, 2.12; N, 6.94; Cu, 7.87; Mo, 29.70. Found: C, 17.85; H, 2.14; N, 6.92; Cu, 7.88; Mo, 29.66. IR (KBr, cm^{-1}): 3430 (w), 3082 (m), 1684 (s), 1633 (w), 1565 (m), 1497 (m), 1440 (m), 1307 (w), 1278 (w), 1169 (w), 1133 (m), 1058 (s), 1035 (m), 1003 (m), 928 (s), 904 (s), 758 (m), 682 (s), 525 (w).

2.4 Synthesis of $[Cu(L)_2(H_2O)]H_2[Cu(L)_2(P_2Mo_5O_{23})]\cdot 4H_2O/Fe_3O_4$

$[Cu(L)_2(H_2O)]H_2[Cu(L)_2(P_2Mo_5O_{23})]\cdot 4H_2O/Fe_3O_4$ nanocomposites were prepared by an ultrasonic procedure. A typical synthesis was carried out in a 50 mL beaker, Fe_3O_4 nanoparticles (5 mg), $[Cu(L)_2(H_2O)]H_2[Cu(L)_2(P_2Mo_5O_{23})]\cdot 4H_2O$ powders (50 mg) were added in a beaker containing water (10 mL) and ethanol (10 mL) in sequence and obtained an uniform and turbid liquid by ultrasound about 10 h. After the completion of the reaction, the resulting products was collected using a magnet putting on one side of the beaker to seperate them from the turbid liquid. The magnetic products were $[Cu(L)_2(H_2O)]H_2[Cu(L)_2(P_2Mo_5O_{23})]\cdot 4H_2O/Fe_3O_4$ nanocomposites, which was washed with water several times.

2.5 Structural characterization and measurements of the nanocomposites

The structures of the synthesized Fe_3O_4 nanoparticles, $[Cu(L)_2(H_2O)]H_2[Cu(L)_2(P_2Mo_5O_{23})]\cdot 4H_2O$ and $[Cu(L)_2(H_2O)]H_2[Cu(L)_2(P_2Mo_5O_{23})]\cdot 4H_2O/Fe_3O_4$ nanocomposites were analyzed by X-ray powder diffraction (XRD, X'Pert Pro) and transmission electron microscopy (TEM, JEOL2010F). The UV-vis spectra were measured by an ultraviolet-visible light absorbance spectrometry (UV-vis, HitachiU4100). In the Fourier transform infrared spectroscopy (FTIR) studies, Fe_3O_4 nanoparticles, $[Cu(L)_2(H_2O)]H_2[Cu(L)_2(P_2Mo_5O_{23})]\cdot 4H_2O$ and $[Cu(L)_2(H_2O)]H_2[Cu(L)_2(P_2Mo_5O_{23})]\cdot 4H_2O/Fe_3O_4$ nanocomposites were separately crushed with a pestle in an agate mortar. The individually crushed material was mixed with KBr in about 1 : 100 proportion. The mixture was then compressed into a 2 mm semi-transparent disk by applying a force of 10 T for 2 min. The Fourier transform infrared spectra were recorded in the wavelength range of 500–4000 cm^{-1} using an Avatar 360 FTIR spectrometer (FTIR, Nicolet Company, USA). The magnetic properties were subsequently investigated by a vibrating sample magnetometry (VSM, Lakeshore 7300).

2.6 Crystallography

Crystallographic data were collected with a Bruker SMART-CCD APEX II diffractometer with graphite-monochromated Mo Kα radiation (λ = 0.71073 Å). The structures were solved by direct methods and refined by full-matrix least squares on F^2 with

Table 1 Summary of crystal data and refinement results for $[Cu(L)_2(H_2O)]H_2[Cu(L)_2(P_2Mo_5O_{23})]\cdot 4H_2O$

Crystal data	$[Cu(L)_2(H_2O)]H_2[Cu(L)_2(P_2Mo_5O_{23})]\cdot 4H_2O$
Empirical formula	$C_{24}H_{34}Cu_2Mo_5N_8O_{32}P_2$
f_w	1615.30
Cryst syst	Triclinic
Space group	$P\bar{1}$
T (K)	296(2)
a (Å)	10.187(3)
b (Å)	10.918(3)
c (Å)	20.739(5)
α (deg)	82.052(4)
β (deg)	89.700(5)
γ (deg)	88.467(5)
V (Å^3)	2283.6(10)
Z	2
D_c (g cm^{-3})	2.335
μ (mm^{-1})	2.423
Crystal size (mm)	$0.27 \times 0.18 \times 0.15$
θ (deg)	1.983–25.098
$F(000)$	1556
hkl range	$-12 \leq h \leq 9$,
	$-12 \leq k \leq 12$,
	$-24 \leq l \leq 24$
GOF on F^2	0.999
R_{int}	0.0433
No. param	671
Refl. measured/unique	8012/5810
R_1, wR_2 $[I \geq 2\sigma(I)]$	0.0551, 0.1396
R_1, wR_2 (all data)	0.0818, 0.1601
$\Delta\rho_{max}$, $\Delta\rho_{min}$ (e Å^{-3})	1.821, -1.678

anisotropic displacement parameters for all non-hydrogen atoms using SHELXTL.[29] The hydrogen atoms are added in idealized geometrical positions. Crystal data, experimental details, and refinement results are listed in Table 1.

2.7 Characterization of adsorption activity

The adsorption activities of the nanocomposites were performed in the dark by measuring the adsorption rate of different dye solutions at room temperature. The dye solutions such as methylene blue, gentian violet, safranine T and fuchsin basic, methyl orange and Sudan red (III) were prepared with a concentration of 15 mg L^{-1} by dissolving the dye powder in distilled water. The reaction was conducted with 5 mg of $[Cu(L)_2(H_2O)]H_2[Cu(L)_2(P_2Mo_5O_{23})]\cdot 4H_2O/Fe_3O_4$ nanocomposites which is the adsorbents dispersed in 30 mL of 15 mg L^{-1} each dye solutions. After stirring, the samples (volume of each is about 5 mL) were drawn out from the reaction beaker every a period of time, centrifuged at 4500 rpm for 10 min and filtered to remove the particles. The filtrate was then analyzed using a UV-vis spectrophotometer (Beijingpuxitongyong TU-1900) to measure the absorption of different dyes.

2.8 Characterization of desorption, reusability activities

In order to investigate the regeneration of the adsorbents during the adsorption experiments, a solvent DMF is chosen as the eluents. The stability and reusability of the nanocomposites on removing fuchsin basic were investigated through cycle tests. The fuchsin basic solution was prepared with a concentration of

15 mg L^{-1} by dissolving the dye powder in distilled water. The reaction was conducted with 50 mg of the adsorbents dispersed in 20 mL of 15 mg L^{-1} fuchsin basic. After each cycle, the adsorbents were separated from aqueous solution by a piece of magnet and washed with a solvent DMF about 20 mL at room temperature to remove the adsorbed fuchsin basic. Then, the regenerated $[Cu(L)_2(H_2O)]H_2[Cu(L)_2(P_2Mo_5O_{23})]\cdot 4H_2O/Fe_3O_4$ nanocomposites were added to the initial dye solution of fuchsin basic (20 mL of 15 mg L^{-1}). The concentrations of fuchsin basic solution were determined by measuring the absorbance through a UV-vis spectrophotometer (Beijingpuxitongyong TU-1900).

3 Results and discussion

3.1 Crystal structure description of compound $[Cu(L)_2(H_2O)]$ $H_2[Cu(L)_2(P_2Mo_5O_{23})]\cdot 4H_2O$

Selected bond distances and angles of $[Cu(L)_2(H_2O)]H_2$-$[Cu(L)_2(P_2Mo_5O_{23})]\cdot 4H_2O$ are given in Table 2. The molecular structures along with the atom numbering scheme are depicted in Fig. 1.

Table 2 Selected bond lengths (Å) and angles (deg) for $[Cu(L)_2(H_2O)]$ $H_2[Cu(L)_2(P_2Mo_5O_{23})]\cdot 4H_2O$

$[Cu(L)_2(H_2O)]H_2[Cu(L)_2(P_2Mo_5O_{23})]\cdot 4H_2O$

Cu(1)–O(1)	1.967(6)	Cu(2)–O(3)	1.929(6)
Cu(1)–O(2)	1.959(6)	Cu(2)–O(4)	1.949(6)
Cu(1)–N(1)	1.964(7)	Cu(2)–O(5)	2.236(6)
Cu(1)–N(3)	1.987(8)	Cu(2)–N(5)	1.985(7)
Cu(1)–O(1W)	2.171(6)	Cu(2)–N(7)	1.958(7)
O(1)–Cu(1)–N(3)	97.1(3)	O(3)–Cu(2)–O(4)	168.9(3)
O(1)–Cu(1)–O(1W)	98.6(3)	O(3)–Cu(2)–O(5)	94.5(3)
O(2)–Cu(1)–O(1)	164.5(3)	O(3)–Cu(2)–N(5)	82.4(3)
O(2)–Cu(1)–N(1)	96.0(3)	O(3)–Cu(2)–N(7)	95.4(3)
N(1)–Cu(1)–N(3)	82.6(3)	O(4)–Cu(2)–O(5)	96.5(3)
O(2)–Cu(1)–O(1W)	96.8(3)	O(4)–Cu(2)–N(5)	98.2(3)
N(1)–Cu(1)–O(1)	82.5(3)	O(4)–Cu(2)–N(7)	82.7(3)
N(1)–Cu(1)–N(3)	173.2(3)	N(5)–Cu(2)–O(5)	81.7(3)
N(1)–Cu(1)–O(1W)	92.1(3)	N(7)–Cu(2)–O(5)	105.7(3)
N(3)–Cu(1)–O(1W)	94.6(3)	N(7)–Cu(2)–N(5)	172.4(3)
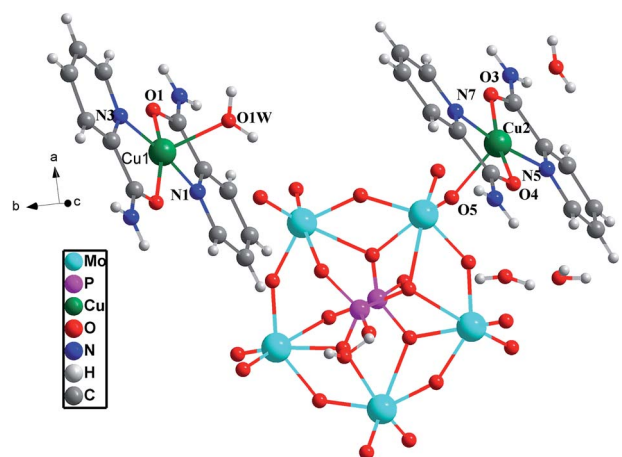
Fig. 1 Structure of $[Cu(L)_2(H_2O)]H_2[Cu(L)_2(P_2Mo_5O_{23})]\cdot 4H_2O$ with atomic numbering scheme.

Single-crystal X-ray structural analysis exhibits that $[(CuL_2)(H_2O)]H_2[(CuL_2)(P_2Mo_5O_{23})]\cdot4H_2O$ crystallizes in $P\bar{1}$ space group. In addition, Fig. 1a shows that compound $[(CuL_2)(H_2O)]$ $H_2[(CuL_2)(P_2Mo_5O_{23})]\cdot4H_2O$ consists of $[(CuL_2)(P_2Mo_5O_{23})]^{4-}$ polyanion, $[CuL_2]^{2+}$ complex fragments and four water molecules in the structural unit of compound $[(CuL_2)(H_2O)]H_2[(CuL_2)(P_2Mo_5O_{23})]\cdot4H_2O$. As is well known, the P_2Mo_5 cluster can be viewed as two $\{PO_4\}$ tetrahedral capping either side of an irregular ring of five distorted $\{MoO_6\}$ octahedral linked by one corner-shared and four edge-shared contacts. Each phosphate subunit shares three oxo-groups with the molybdate ring. One of these oxo-groups adopts a μ_2-bridging mode, linking one molybdenum atom and a phosphorus atom; while the other two adopt a μ_3-bridging mode, linking two molybdenum atoms and a phosphorus atom.[30] Each of two Cu atoms adopts a five-coordinated distorted $\{CuN_2O_3\}$ square-pyramidal geometry surrounded by two pyridine-2-carboxamide ligands and one O atom from P_2Mo_5 cluster or one water, respectively. The Cu(1) is coordinated by two N (amide) atoms with Cu–N bond lengths of 1.968(9)–1.970(9) Å, two O (amide) atoms with Cu–O bond lengths of 1.958(7)–1.960(7) Å and one O (aqua) atom with Cu–Ow bond lengths of 2.169(7) Å. The Cu(2) atom is coordinated by two N (amide) atoms with Cu–N bond lengths of 1.961 (9)–1.978(9) Å, one O atom of $\{MoO_6\}$ octahedron with Cu–O bond lengths of 2.231(7) Å, and two O (amide) atom with Cu–O bond lengths of 1.930(7)–1.945(7) Å.[31]

3.2 IR spectroscopy

Fig. 2 compares the FTIR spectra of Fe_3O_4 nanoparticles, $[Cu(L)_2(H_2O)]H_2[Cu(L)_2(P_2Mo_5O_{23})]\cdot4H_2O$ and $[Cu(L)_2(H_2O)]H_2$-$[Cu(L)_2(P_2Mo_5O_{23})]\cdot4H_2O/Fe_3O_4$ nanocomposites. In Fig. 2b, the Fe_3O_4 nanoparticles show one strong characteristic band at the position of 600 cm^{-1} which is associated with the stretching vibration mode of Fe–O.[32–34] The IR spectrum of $[Cu(L)_2(H_2O)]H_2$-$[Cu(L)_2(P_2Mo_5O_{23})]\cdot4H_2O$ has been depicted in Fig. 2c. It is evident that the characteristic band at 3378 cm^{-1} is attributed to the O–H stretching vibration of water, while the peaks at 3072 cm^{-1} are related to the ν(N–H) of pyridine-2-carboxamide. A series of strong bands in the range of 1684–1133 cm^{-1} is also associated with pyridine-2-carboxamide. Bands in the region of 1120–1008 cm^{-1} are assigned to ν(P–O) stretching vibration.[35,36] The peaks at 908 cm^{-1} and 672 cm^{-1} are attributed to ν(Mo = O_d) and ν(Mo–O–Mo), respectively.[36] As given in Fig. 2a, these characteristic vibration and bending modes reappear in the FTIR spectrum of the $[Cu(L)_2(H_2O)]H_2[Cu(L)_2(P_2Mo_5O_{23})]\cdot4H_2O/Fe_3O_4$, but instead shifting to the positions of 3389 cm^{-1} for the O–H stretching vibration and 3174 cm^{-1} for the ν(N–H) of pyridine-2-carboxamide. The result is that Fe_3O_4 and $[Cu(L)_2(H_2O)]H_2[Cu(L)_2(P_2Mo_5O_{23})]\cdot4H_2O$ are existed in $[Cu(L)_2(H_2O)]H_2[Cu(L)_2(P_2Mo_5O_{23})]\cdot4H_2O/Fe_3O_4$ nanocomposites, which demonstrates the synthesis of $[Cu(L)_2(H_2O)]H_2[Cu(L)_2(P_2Mo_5O_{23})]\cdot4H_2O/Fe_3O_4$ nanocomposites.

3.3 UV-vis spectroscopy

The optical property of $[Cu(L)_2(H_2O)]H_2[Cu(L)_2(P_2Mo_5O_{23})]\cdot4H_2O/Fe_3O_4$ were assessed by UV-visible absorption spectroscopy. Fig. 3a–c shows the UV-vis spectra of $[Cu(L)_2(H_2O)]H_2$-$[Cu(L)_2(P_2Mo_5O_{23})]\cdot4H_2O/Fe_3O_4$ nanocomposites, $[Cu(L)_2(H_2O)]$
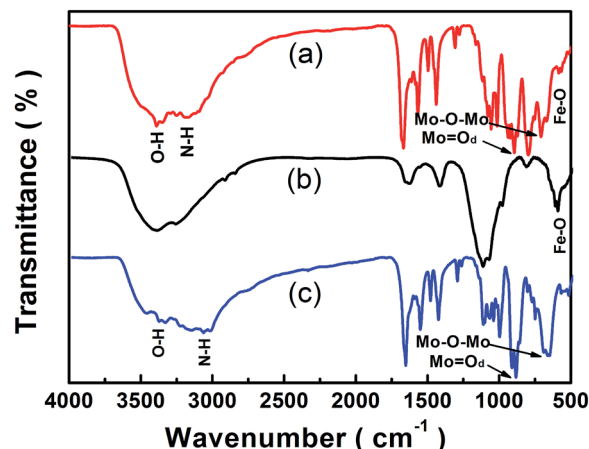
Fig. 2 FTIR spectra of $[Cu(L)_2(H_2O)]H_2[Cu(L)_2(P_2Mo_5O_{23})]\cdot4H_2O/$ Fe_3O_4 (a), Fe_3O_4 (b) and $[Cu(L)_2(H_2O)]H_2[Cu(L)_2(P_2Mo_5O_{23})]\cdot4H_2O$ (c).

$H_2[Cu(L)_2(P_2Mo_5O_{23})]\cdot4H_2O$ and Fe_3O_4 dispersed in H_2O. Apparently, in Fig. 3b, $[Cu(L)_2(H_2O)]H_2[Cu(L)_2(P_2Mo_5O_{23})]\cdot4H_2O$ shows two of absorption bands, and the absorption bands observed around 211 nm and 264 nm, which are attributed to the charge-transfer of $O_t \rightarrow Mo$ and $O_b \rightarrow Mo$, respectively.[37] As given in Fig. 3c, in the ultraviolet and visible light area, Fe_3O_4 nanoparticles have no obvious absorption bands. Clearly, in Fig. 3a, there are two kinds of absorption bands, one at about 210 nm and the other at about 265 nm, both from $[Cu(L)_2(H_2O)]H_2[Cu(L)_2(P_2Mo_5O_{23})]\cdot4H_2O$, the peak pattern of $[Cu(L)_2(H_2O)]H_2[Cu(L)_2(P_2Mo_5O_{23})]\cdot4H_2O/Fe_3O_4$ nanocomposites is similar to that of $[Cu(L)_2(H_2O)]H_2[Cu(L)_2(P_2Mo_5O_{23})]\cdot4H_2O$, and the position of the two peaks is nearly alike, and coming about shift slightly is due to the existence of Fe_3O_4 nanoparticles.

3.4 TEM morphology and particle size distribution of $[Cu(L)_2(H_2O)]H_2[Cu(L)_2(P_2Mo_5O_{23})]\cdot4H_2O/Fe_3O_4$

The morphology, nanostructure, particle size and size distribution of the prepared $[Cu(L)_2(H_2O)]H_2[Cu(L)_2(P_2Mo_5O_{23})]\cdot4H_2O/Fe_3O_4$
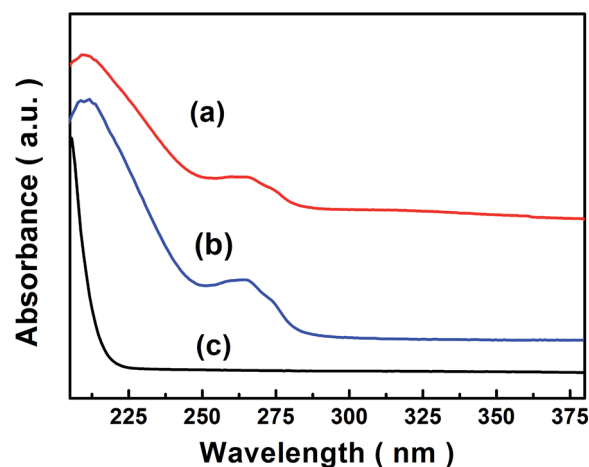
Fig. 3 UV-visible absorbance spectra of $[Cu(L)_2(H_2O)]H_2[Cu(L)_2(P_2$-$Mo_5O_{23})]\cdot4H_2O/Fe_3O_4$ (a), $[Cu(L)_2(H_2O)]H_2[Cu(L)_2(P_2Mo_5O_{23})]\cdot4H_2O$ (b) and Fe_3O_4 (c) dispersed in H_2O.
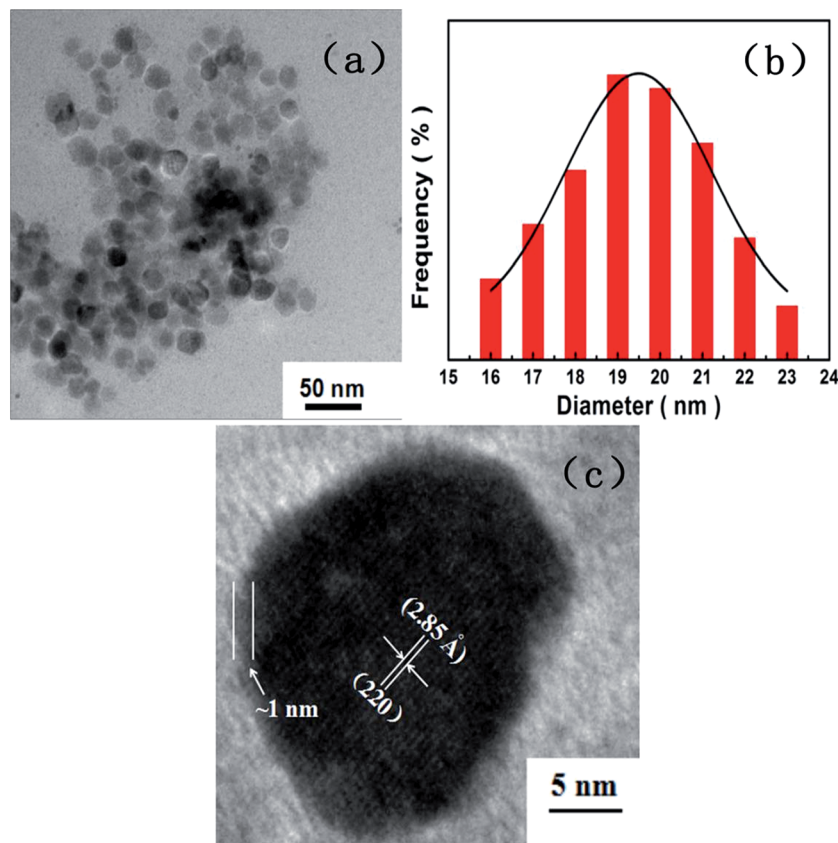
Fig. 4   TEM analyses (a), particle size histogram with Gaussian fit (b) and HRTEM analyses of $[Cu(L)_2(H_2O)]H_2[Cu(L)_2(P_2Mo_5O_{23})]\cdot4H_2O/Fe_3O_4$ nanocomposites (c).

nanocomposites were recorded by TEM and HRTEM. As given in Fig. 4a, the obtained $[Cu(L)_2(H_2O)]H_2[Cu(L)_2(P_2Mo_5O_{23})]\cdot4H_2O/Fe_3O_4$ nanocomposites are virtually uniform and nearly spherical in shape with seldom aggregation. The histograms in Fig. 4b shows the size distribution of $[Cu(L)_2(H_2O)]H_2[Cu(L)_2(P_2Mo_5O_{23})]\cdot4H_2O/Fe_3O_4$ nanocomposites, which are reasonably described by the Gaussian function, showing tight size distribution with average sizes of approximately 19.43 nm in diameter. Fig. 4c represents the HRTEM image of a single $[Cu(L)_2(H_2O)]$

$H_2[Cu(L)_2(P_2Mo_5O_{23})]\cdot4H_2O/Fe_3O_4$ nanocomposite. As labeled, the spacing of 2.85 Å corresponds to the (220) reflection of the Fe_3O_4 phase. Moreover, with a higher magnification than in Fig. 4a of the same sample, a thin layer with ~1 nm uneven thickness is clearly observed in Fig. 4c. We think that this similarly may be the example of observation of such kind of $[Cu(L)_2(H_2O)]$ $H_2[Cu(L)_2(P_2Mo_5O_{23})]\cdot4H_2O/Fe_3O_4$ core–shell structure.[38,39]

3.5   XRD patterns

As shown in Fig. 5, the structure of the $[Cu(L)_2(H_2O)]H_2[Cu(L)_2(P_2Mo_5O_{23})]\cdot4H_2O/Fe_3O_4$ nanocomposites was recorded by XRD
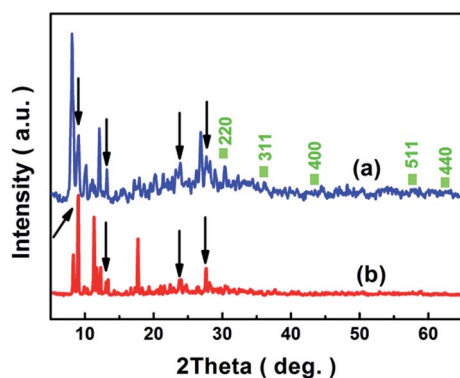
Fig. 5   XRD patterns for $[Cu(L)_2(H_2O)]H_2[Cu(L)_2(P_2Mo_5O_{23})]\cdot4H_2O/Fe_3O_4$ (a), $[Cu(L)_2(H_2O)]H_2[Cu(L)_2(P_2Mo_5O_{23})]\cdot4H_2O$ (b) and squares for the JCPDS of Fe_3O_4.
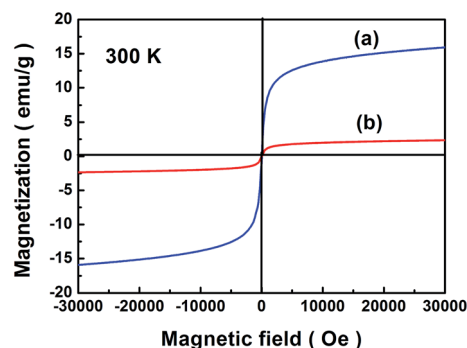
Fig. 6   Magnetic measurements of Fe_3O_4 nanoparticles (a) and $[Cu(L)_2(H_2O)]H_2[Cu(L)_2(P_2Mo_5O_{23})]\cdot4H_2O/Fe_3O_4$ nanocomposites (b).

and analyzed together with the results of Fe_3O_4 and $[Cu(L)_2(H_2O)]$ $H_2[Cu(L)_2(P_2Mo_5O_{23})]\cdot4H_2O$. Fig. 5a represents the diffraction pattern obtained from the $[Cu(L)_2(H_2O)]H_2[Cu(L)_2(P_2Mo_5O_{23})]\cdot4H_2O/Fe_3O_4$ nanocomposites, in match to the standard diffraction peaks of the corresponding Fe_3O_4 (JCPDS No.88-0315), the diffraction peaks positioning at 30.2°, 35.6°, 43.2°, 57.3° and 62.7° are indexed to the (220), (311), (400), (511) and (440) planes

of the Fe_3O_4 nanoparticles. Fig. 5b represents the diffraction pattern obtained from the $[Cu(L)_2(H_2O)]H_2[Cu(L)_2(P_2Mo_5O_{23})]\cdot4H_2O$, the diffraction peaks positioning at 8.8°, 12.9°, 23.8° and 27.1° also appear in Fig. 5a which are indicated by arrows. In conclusion, $[Cu(L)_2(H_2O)]H_2[Cu(L)_2(P_2Mo_5O_{23})]\cdot4H_2O$ and Fe_3O_4 are included in $[Cu(L)_2(H_2O)]H_2[Cu(L)_2(P_2Mo_5O_{23})]\cdot4H_2O/Fe_3O_4$ nanocomposites.

3.6 Magnetic property of $[Cu(L)_2(H_2O)]$ $H_2[Cu(L)_2(P_2Mo_5O_{23})]\cdot4H_2O/Fe_3O_4$

The magnetic property of $[Cu(L)_2(H_2O)]H_2[Cu(L)_2(P_2Mo_5O_{23})]\cdot4H_2O/Fe_3O_4$ nanocomposites was studied by VSM. Fig. 6a and b show the hysteresis curves of Fe_3O_4 nanoparticles and $[Cu(L)_2(H_2O)]H_2[Cu(L)_2(P_2Mo_5O_{23})]\cdot4H_2O/Fe_3O_4$ nanocomposites at 300 K, respectively. It is clear that $[Cu(L)_2(H_2O)]H_2[Cu(L)_2(P_2Mo_5O_{23})]\cdot4H_2O/Fe_3O_4$ nanocomposites show superparamagnetic behavior with a coercivity tend to ~9.0 Oe and magnetization of ~2.37 emu g^{-1} comparing with a coercivity tend to ~0 Oe and magnetization of ~16.10 emu g^{-1} of Fe_3O_4 nanoparticles.

3.7 Separation and aggregation process of $[Cu(L)_2(H_2O)]$ $H_2[Cu(L)_2(P_2Mo_5O_{23})]\cdot4H_2O/Fe_3O_4$

Fig. 7 visually demonstrates the separation and aggregation process of the $[Cu(L)_2(H_2O)]H_2[Cu(L)_2(P_2Mo_5O_{23})]\cdot4H_2O/Fe_3O_4$ nanocomposites in water.[40] Under the influence of an external magnetic field, $[Cu(L)_2(H_2O)]H_2[Cu(L)_2(P_2Mo_5O_{23})]\cdot4H_2O/Fe_3O_4$

Fig. 7 Photo images of solvent of H_2O dispersion-collection process of the $[Cu(L)_2(H_2O)]H_2[Cu(L)_2(P_2Mo_5O_{23})]\cdot4H_2O/Fe_3O_4$ nanocomposites.
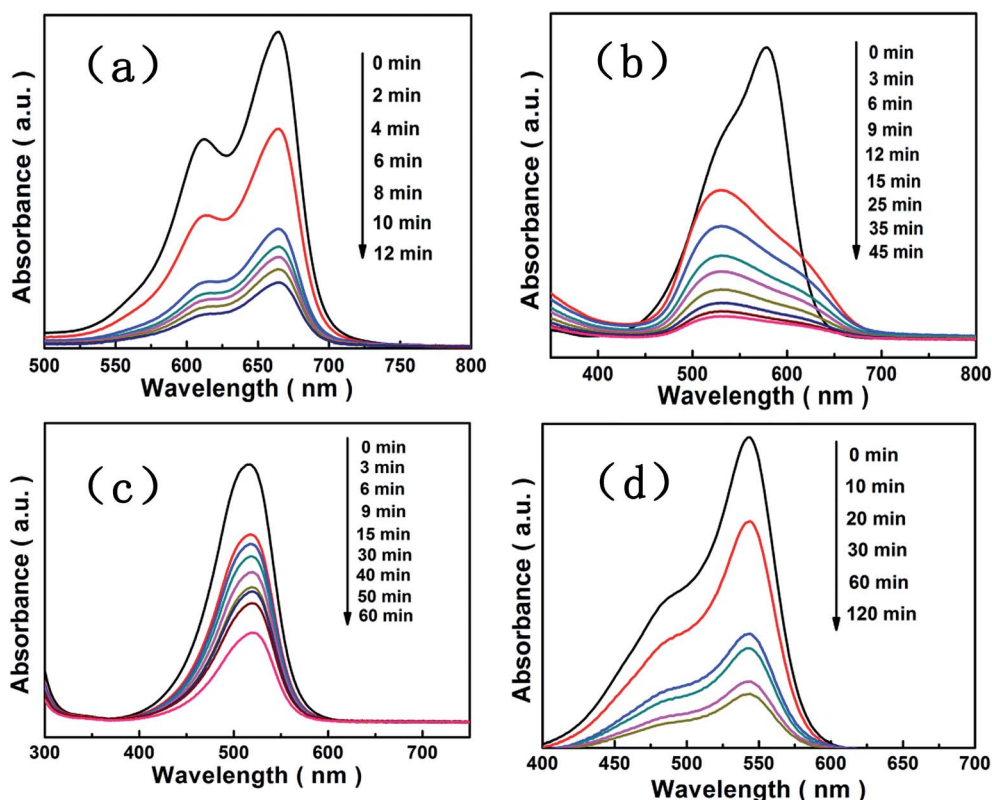

Fig. 8 Adsorption spectra of the methylene blue solution (a), the gentian violet solution (b), the safranine T solution (c) and the fuchsin basic solution (d) under the dark in presence of the $[Cu(L)_2(H_2O)]H_2[Cu(L)_2(P_2Mo_5O_{23})]\cdot4H_2O/Fe_3O_4$ nanocomposites.

nanocomposites in water change from a purplish grey, homogeneous dispersion (Fig. 7a) to a clear, transparent solution, with the nanocomposites collected by a piece of magnet (Fig. 7b). The collected nanocomposites can be easily and reversibly dispersed by agitation after removal of the magnetic field and the above process can be repeated. The finding that all $[Cu(L)_2(H_2O)]H_2[Cu(L)_2(P_2Mo_5O_{23})]\cdot 4H_2O/Fe_3O_4$ nanocomposites as prepared could be collected by a magnet, leaving no free $[Cu(L)_2(H_2O)]H_2[Cu(L)_2(P_2Mo_5O_{23})]\cdot 4H_2O$ visible. In other words, we performed magnetic separation and found that all nanocomposites were collected by the magnet because the $[Cu(L)_2(H_2O)]H_2[Cu(L)_2(P_2Mo_5O_{23})]\cdot 4H_2O/Fe_3O_4$ nanocomposites are magnetic and there is no more nanoparticles left-over, so nonmagnetic $[Cu(L)_2(H_2O)]H_2[Cu(L)_2(P_2Mo_5O_{23})]\cdot 4H_2O$ are not present in the samples.

3.8 Adsorption properties

Organic dyes such as methylene blue, gentian violet, safranine T and fuchsin basic are important organic dyes which are widely used as a colorant in textiles and food stuffs the dyes are harmful if swallowed by human beings and animals, causing irritation to the skin, eye and respiratory tract.[41–43] Their breakdown products in the water may be toxic, carcinogenic or mutagenic to life forms, and they have been shown to cause retching, stun, cyanosis, jaundice and tissue necrosis in human. Therefore, an effective and optimal strategy to degrade the dyes rapidly must be developed. In the design of an economical wastewater disposal system, fast adsorption rate is also an important parameter for design and synthesis of the efficient adsorbent.

We investigated the adsorption of $[Cu(L)_2(H_2O)]H_2[Cu(L)_2(P_2Mo_5O_{23})]\cdot 4H_2O/Fe_3O_4$ nanocomposites using organic dyes such as methylene blue, gentian violet, safranine T, fuchsin basic, methyl orange and Sudan red (III) as probe molecules. Fig. 8 show that $[Cu(L)_2(H_2O)]H_2[Cu(L)_2(P_2Mo_5O_{23})]\cdot 4H_2O/Fe_3O_4$ nanocomposites were able to adsorb the methylene blue, gentian violet, safranine T and fuchsin basic efficiently in the dark. The intensity of UV-visible absorption peak of each dyes decreased with the increase of time due to the existence of $[Cu(L)_2(H_2O)]H_2[Cu(L)_2(P_2Mo_5O_{23})]\cdot 4H_2O/Fe_3O_4$ nanocomposites, and the adsorption efficiency

of methylene blue, gentian violet, safranine T and fuchsin basic were 79%, 91%, 64% and 83% in 12 min, 45 min, 60 min and 120 min, respectively. In addition, the peak patterns of each dyes are sightly similar and the peak positions are the same except gentian violet which may be due to itself of gentian violet. Fig. 9 show that $[Cu(L)_2(H_2O)]H_2[Cu(L)_2(P_2Mo_5O_{23})]\cdot 4H_2O/Fe_3O_4$ nanocomposites were not able to adsorb the methyl orange, Sudan red (III) efficiently in the dark. The intensity of UV-visible absorption peak of methyl orange and Sudan red (III) both are almost constant. The reason of the same adsorbent with different effects on removal of dyes is related to the structure of the dye molecules and the structure of the $[Cu(L)_2(H_2O)]H_2[Cu(L)_2(P_2Mo_5O_{23})]\cdot 4H_2O/Fe_3O_4$ nanocomposites.

POMs, as an outstanding family of metal-oxide clusters with controllable shape and size, highly electronegative, and oxo-enriched surfaces, are expected to exhibit good adsorption towards cationic dyes.[44] Firstly, POMs are a kind of hydrophilic metal-oxo cluster compounds. The hydrophilic/hydrophobic property of the framework is modulated by encapsulating the POM molecules, which allows the ingress and egress of the dye molecules. Secondly, POMs with a large number of negative charges encapsulated in the neutral framework may have a stronger force with the positive charges of dyes. The approving
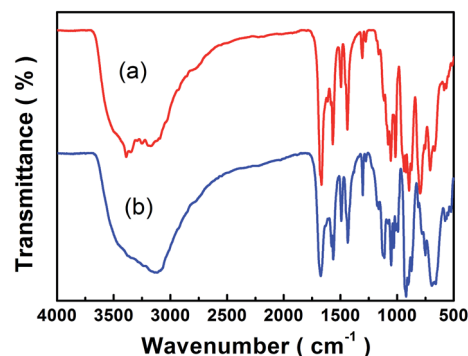

Fig. 10 FTIR spectra as-synthesized (a) and after adsorption and desorption tests (b) of the $[Cu(L)_2(H_2O)]H_2[Cu(L)_2(P_2Mo_5O_{23})]\cdot 4H_2O/Fe_3O_4$ nanocomposites.
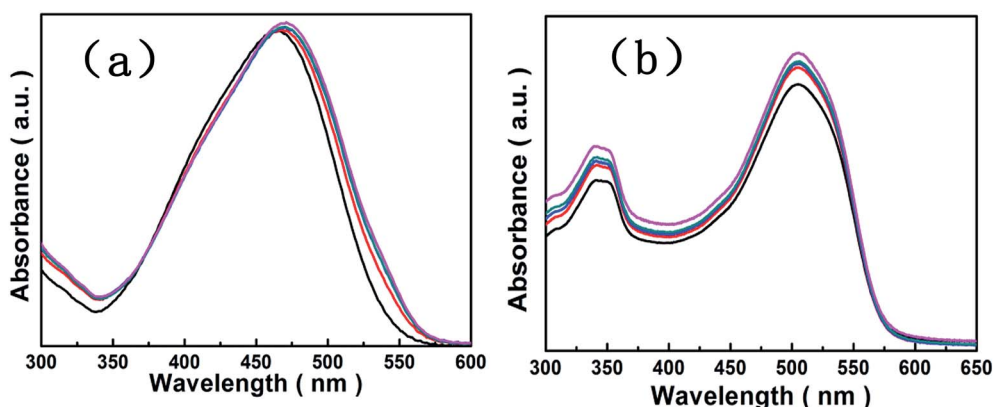

Fig. 9 Adsorption spectra of the methyl orange solution (a) and the Sudan red (III) solution (b) under the dark in presence of the $[Cu(L)_2(H_2O)]H_2[Cu(L)_2(P_2Mo_5O_{23})]\cdot 4H_2O/Fe_3O_4$ nanocomposites.

Fig. 11 The photographs of three adsorption and desorption cycles, the first cycle: Ad-1st and De-1st; the second cycle: Ad-2nd and De-2nd; the third cycle: Ad-3rd and De-3rd.

result is that $[Cu(L)_2(H_2O)]H_2[Cu(L)_2(P_2Mo_5O_{23})]\cdot 4H_2O/Fe_3O_4$ nanocomposites exhibit rapid adsorption efficiency and high uptake capacity towards methylene blue, gentian violet, safranine T and fuchsin basic than methyl orange, Sudan red (III), which is in accord with literature.[45] The magnetic $[Cu(L)_2(H_2O)]$ $H_2[Cu(L)_2(P_2Mo_5O_{23})]\cdot 4H_2O/Fe_3O_4$ nanocomposites combining $[Cu(L)_2(H_2O)]H_2[Cu(L)_2(P_2Mo_5O_{23})]\cdot 4H_2O$ and Fe_3O_4 nanoparticles could be collected in adsorption process preferably.

3.9 Stability and reusability behaviours

The stability and reusability of the nanocomposites are another important standard for practical application. It can be seen from the process of magnetic aggregation and dispersion that the $[Cu(L)_2(H_2O)]H_2[Cu(L)_2(P_2Mo_5O_{23})]\cdot 4H_2O/Fe_3O_4$ are not the mixture of $[Cu(L)_2(H_2O)]H_2[Cu(L)_2(P_2Mo_5O_{23})]\cdot 4H_2O$ and Fe_3O_4 nanoparticles but a new nanocomposite, although it is still a challenge to identify the interaction between POM species and magnetic particles. The in-depth study is on the way. As shown in Fig. 10, the IR patterns of the adsorbents regenerated from adsorption and desorption experiments match well with the as-synthesized product, indicating that the structure of the nanocomposites remain intact, which confirms their good stability and recyclability. The properties are significant in improving the use of material without loss of their structure and reducing the adsorption cost. In a word, the nanocomposites are of great significance for the practical use of the absorbents and exhibit good reproducibility.

After adsorption experiments, the adsorbed fuchsin basic can be removed by a solvent DMF. In Fig. 11, it shows that the photographs of three adsorption and desorption cycles. When a solution of DMF was added, digital images show that fuchsin basic molecules in the nanocomposites can be rapidly released. Then, the regenerated $[Cu(L)_2(H_2O)]H_2[Cu(L)_2(P_2Mo_5O_{23})]\cdot$ $4H_2O/Fe_3O_4$ nanocomposites were added to the initial fuchsin basic solution (20 mL of 15 mg L^{-1}), the adsorbents are still capable of removing fuchsin basic up to 91%, 93% and 90% over one cycles, two cycle, three cycle, respectively, as shown in Fig. 12. This means that the dye release is also an ion-exchange process, which also further demonstrate that ionic interaction between dyes and anionic framework is main determinant for selective adsorption and separation of dyes.[46]
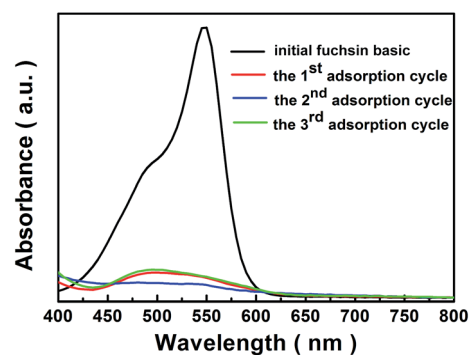

Fig. 12 The UV-vis spectra of initial fuchsin basic, the 1st adsorption cycle, the 2nd adsorption cycle and the 3rd adsorption cycle.

The new $[Cu(L)_2(H_2O)]H_2[Cu(L)_2(P_2Mo_5O_{23})]\cdot 4H_2O/Fe_3O_4$ nanocomposites have been successfully synthesized, and were adopted as adsorbents for the removal of dyes in aqueous solution. Interestingly, they not only exhibit rapid adsorption rate and high uptake capacity towards fuchsin basic, but also realize the recycling performance. This work opens up a useful, economical adsorption and desorption, which can improve the recycling of raw material in wastewater.

4 Conclusions

In summary, we have successfully synthesized the nanocomposites of $[Cu(L)_2(H_2O)]H_2[Cu(L)_2(P_2Mo_5O_{23})]\cdot 4H_2O/Fe_3O_4$ that combining $[Cu(L)_2(H_2O)]H_2[Cu(L)_2(P_2Mo_5O_{23})]\cdot 4H_2O$ and Fe_3O_4 nanoparticles. The morphology and structural analyses reveal the narrow particle size distribution with an average diameter ~19.43 nm and high crystallinity of the nanocomposite. The FTIR and XRD assessments confirm $[Cu(L)_2(H_2O)]H_2[Cu(L)_2$-$(P_2Mo_5O_{23})]\cdot 4H_2O$ and Fe_3O_4 nanoparticles are existed in $[Cu(L)_2(H_2O)]H_2[Cu(L)_2(P_2Mo_5O_{23})]\cdot 4H_2O/Fe_3O_4$ nanocomposites. The UV-vis measurement shows the well-defined optical absorption with the nanocomposites dispersed in H_2O. The magnetic characterization shows that $[Cu(L)_2(H_2O)]H_2[Cu(L)_2(P_2Mo_5O_{23})]\cdot 4H_2O/Fe_3O_4$ nanocomposites have superparamagnetic behavior. The dispersion-collection processes in H_2O of the $[Cu(L)_2(H_2O)]$ $H_2[Cu(L)_2(P_2Mo_5O_{23})]\cdot 4H_2O/Fe_3O_4$ nanocomposites were

demonstrated for application readiness. $[Cu(L)_2(H_2O)]H_2$-$[Cu(L)_2(P_2Mo_5O_{23})]\cdot4H_2O/Fe_3O_4$ nanocomposites have selective adsorption behavior for organic dyes. Meanwhile, the stable and reusable $[Cu(L)_2(H_2O)]H_2[Cu(L)_2(P_2Mo_5O_{23})]\cdot4H_2O/Fe_3O_4$ nanocomposites were found to be a good adsorbent and could be employed as an effective adsorbent applicable in adsorption field.

Acknowledgements

References

1 Z. Ma, Q. Liu, Z. M. Cui, S. W. Bian and W. G. Song, *J. Phys. Chem. C*, 2008, **112**, 8875–8880.

2 M. Huang, L. Bi, Y. Shen, B. Liu and S. Dong, *J. Phys. Chem. B*, 2004, **108**, 9780–9786.

3 Z. Sun, L. Xu, W. Guo, B. Xu, S. Liu and F. Li, *J. Phys. Chem. C*, 2010, **114**(11), 5211–5216.

4 C. Li, K. P. O'Halloran, H. Ma and S. Shi, *J. Phys. Chem. B*, 2009, **113**, 8043–8048.

5 J. Kim, L. Lee, B. K. Niece, J. X. Wang and A. A. Gewirth, *J. Phys. Chem. B*, 2004, **108**, 7927–7933.

6 D. An, A. Ye, W. Deng, Q. Zhang and Y. Wang, *Chem.–Eur. J.*, 2012, **18**, 2938–2947.

7 S. Li, X. Yu, G. Zhang, Y. Ma, J. Yao and P. de Oliveira, *Carbon*, 2011, **49**, 1906–1911.

8 A. Troupis, A. Hiskia and E. Papaconstantinou, *Angew. Chem., Int. Ed.*, 2002, **41**(11), 1911–1914.

9 E. Tebandeke, C. Coman, K. Guillois, G. Canning, E. Ataman, J. Knudsen, L. R. Wallenberg, H. Ssekaalo, J. Schnadt and O. F. Wendt, *Green Chem.*, 2014, **16**, 1586–1593.

10 A. Babakhanian, S. Kaki, M. Ahmadi, H. Ehzari and A. Pashabadi, *Biosens. Bioelectron.*, 2014, **60**, 185–190.

11 H. K. Daima, P. R. Selvakannan, R. Shukla, S. K. Bhargava and V. Bansal, *PLoS One*, 2013, **8**, e79676.

12 W. Zheng, L. Yang, Y. Liu, X. Qin, Y. Zhou, Y. Zhou and J. Liu, *Sci. Technol. Adv. Mater.*, 2014, **15**, 035010.

13 Y. Kikukawa, Y. Kuroda, K. Yamaguchi and N. Mizuno, *Angew. Chem.*, 2012, **124**, 2484–2487.

14 U. Kortz, A. Müeller, J. van Slageren, J. Schnack, N. S. Dalal and M. Dressel, *Coord. Chem. Rev.*, 2009, **253**, 2315–2327.

15 H. N. Miras, J. Yan, D. L. Long and L. Cronin, *Chem. Soc. Rev.*, 2012, **41**, 7403–7430.

16 K. M. Seemann, M. Luysberg, Z. Révay, P. Kudejova, B. Sanz, N. Cassinelli, A. Loidl, K. Llicic, G. Multhoff and T. E. Schmid, *J. Controlled Release*, 2015, **197**, 131–137.

17 Z. You, Y. Chen, T. Liu, Z. Yang, F. Xie and Y. Sun, *Inorg. Chim. Acta*, 2014, **421**, 160–168.

18 S. Saif, A. Tahir and Y. Chen, *Nanomaterials*, 2016, **6**, 209.

19 H. L. Liu, J. H. Wu, J. H. Min and Y. K. Kim, *J. Alloys Compd.*, 2012, **537**, 60–64.

20 H. L. Liu, J. H. Wu, J. H. Min, X. Y. Zhang and Y. K. Kim, *Mater. Res. Bull.*, 2013, **48**, 551–558.

21 H. L. Liu, P. Hou, W. X. Zhang and J. H. Wu, *Colloids Surf.*, 2010, **356**(1), 21–27.

22 H. L. Liu, S. P. Ko, J. H. Wu, M. H. Jung, J. H. Min, J. H. Lee, B. H. An and Y. K. Kim, *J. Magn. Magn. Mater.*, 2007, **310**(2), e815–e817.

23 S. Lin, Z. Song, G. Che, A. Ren, P. Li, C. Liu and J. Zhang, *Microporous Mesoporous Mater.*, 2014, **193**, 27–34.

24 A. Dandia, V. Parewa, A. K. Jain and K. S. Rathore, *Green Chem.*, 2011, **13**, 2135.

25 B. Adhikari, G. Palui and A. Banerjee, *Soft Matter*, 2009, **5**, 3452–3460.

26 J. Thomas and A. Ramanan, *Inorg. Chim. Acta*, 2011, **372**, 243–249.

27 M. Ðaković, Z. Popović, G. Giester and M. Rajić-Linarić, *Polyhedron*, 2008, **27**, 210–222.

28 H. Paşaoğlu, S. Güven, Z. Heren and O. Büyükgüngör, *J. Mol. Struct.*, 2006, **794**, 270–276.

29 G. M. Sheldrick, *Acta Crystallogr., Sect. A: Found. Crystallogr.*, 2008, **64**(1), 112–122.

30 J. X. Meng, Y. Lu, Y. G. Li, H. Fu and E. B. Wang, *CrystEngComm*, 2011, **13**, 2479–2486.

31 H. J. Jin, B. B. Zhou, Y. Yu, Z. F. Zhao and Z. H. Su, *CrystEngComm*, 2011, **13**, 585–590.

32 R. Yuvakkumar and S. I. Hong, *Adv. Mater. Res.*, 2014, **1051**, 39–42.

33 Y. P. Yew, K. Shameli, M. Miyake, N. Kuwano, N. B. B. A. Khairudin, S. E. B. Mohamad and K. X. Lee, *Nanoscale Res. Lett.*, 2016, **11**(1), 1–7.

34 S. H. Ahmadi, P. Davar and A. Manbohi, *Iran. J. Chem. Chem. Eng.*, 2016, **35**, 63–73.

35 Z. L. Li, Y. Wang, L. C. Zhang, J. P. Wang, W. S. You and Z. M. Zhu, *Dalton Trans.*, 2014, **43**, 5840–5846.

36 B. D'Cruz, J. Samuel and L. George, *Thermochim. Acta*, 2014, **596**, 29–36.

37 L. H. Wei, Z. L. Wang, J. W. Zhao and J. P. Wang, *Chin. J. Struct. Chem.*, 2010, **29**, 784–788.

38 G. Zhang, B. Keita, A. Dolbecq, P. Mialane, F. Sécheresse, F. Miserque and L. Nadjo, *Chem. Mater.*, 2007, **19**, 5821–5823.

39 A. Neyman, L. Meshi, L. Zeiri and I. A. Weinstock, *J. Am. Chem. Soc.*, 2008, **130**, 16480–16481.

40 H. L. Liu, J. H. Wu, J. H. Min, P. Hou, A. Y. Song and Y. K. Kim, *Nanotechnology*, 2010, **22**, 055701.

41 S. Thakur, S. Pandey and O. A. Arotiba, *Carbohydr. Polym.*, 2016, **153**, 34–46.

42 K. A. G. Gusmão, L. V. A. Gurgel, T. M. S. Melo and L. F. Gil, *J. Environ. Manage.*, 2013, **118**, 135–143.

43 X. Xu, B. Bai, H. Wang and Y. Suo, *J. Phys. Chem. Solids*, 2015, **87**, 23–31.

44 A. X. Yan, S. Yao, Y. G. Li, Z. M. Zhang, Y. Lu, W. L. Chen and E. B. Wang, *Chem.–Eur. J.*, 2014, **20**, 6927–6933.

45 F. Y. Yi, W. Zhu, S. Dang, J. P. Li, D. Wu, Y. H. Li and Z. M. Sun, *Chem. Commun.*, 2015, **51**, 3336–3339.

46 J. S. Qin, S. R. Zhang, D. Y. Du, P. Shen, S. J. Bao, Y. Q. Lan and Z. M. Su, *Chem.–Eur. J.*, 2014, **20**, 5625–5630.